Title

Complete miscibility of immiscible elements at the nanometre scale

Journal

Nature Nanotechnology, 19(6)

ISSN

1748-3387

Authors

Chen, Peng-Cheng

Gao, Mengyu

McCandler, Caitlin A

et al.

Publication Date

2024-06-01

DOI

10.1038/s41565-024-01626-0

Peer reviewed

Complete miscibility of immiscible elements at the nanometer scale

Peng-Cheng Chen[1,2,†,‡], Mengyu Gao[3,‡], Caitlin A. McCandler[1,3,‡], Chengyu Song[4], Jianbo Jin[2], Yao Yang[2,5], Arifin Luthfi Maulana[3], Kristin A. Persson[1,3,4], Peidong Yang[1,2,3*]

[1]Kavli Energy Nanoscience Institute, [2]Department of Chemistry, [3]Department of Materials Science and Engineering, University of California, Berkeley, California 94720, United States.

[4]Molecular Foundry, Lawrence Berkeley National Laboratory, Berkeley, California 94720, United States

[5]Miller Institute, University of California, Berkeley, California 94720, United States.

†Present address: Department of Materials Science, Fudan University, Shanghai 200438, China

‡These authors contributed equally to this work.

*Corresponding author. Email: p_yang@berkeley.edu

Abstract

Understanding the mixing behavior of elements in a multielement material is important to control its structure and property. When the size of a multielement material is decreased to the nanoscale, the miscibility of elements in the nanomaterial often changes from its bulk counterpart. However, there is a lack of comprehensive and quantitative experimental insights into this process. Here we explored how the miscibility of Au and Rh evolves in nanoparticles of size varying from 4 to 1 nm and composition changing from 15%Au to 85%Au. We found that the two immiscible elements exhibit a phase separation-to-alloy transition in nanoparticles with decreased size and become completely miscible in sub-2 nm particles across the entire compositional range. Quantitative electron microscopy analysis and theoretical calculations were used to show that the observed immiscibility-to-miscibility transition is dictated by particle size, composition, and possible surface adsorbates present under synthesis conditions.

Multielement materials are of particular interest in catalysis[1,2], structural materials[3-5], optoelectronic devices[6,7], thermal energy harvesting[8,9], quantum computing[10], etc. The chemical, mechanical, and electronic interplay between multiple elements in a material, either in an alloyed or phase-separated format, allows the material to harness multielement synergy to achieve enhanced properties. Controlling the alloying and phase-separation behavior of elements, usually guided by the bulk phase diagrams[11], is a prerequisite to realize those target properties. Compared with bulk scale, miniaturizing the dimensions of multielement materials to the nanoscale can often significantly change their physical and chemical properties. In particular, novel multielement nanomaterials have been systematically created[12-21] and new properties have been identified for a variety of applications[1,2,6,7,10,22-25].

At the same time, researchers have noticed that the bulk phase diagram may not apply at the nanoscale. For example, theoretical simulations on nanoparticles composed of immiscible elements have unveiled the shrinking of the miscibility gap in the size regime of 1-10 nm[26-29]. Further, mixing of immiscible elements such as Ag-Ni, Ag-Cu, Au-Rh, and Au-Pt have been experimentally observed in nanomaterials made by colloidal co-reduction synthesis[13,30-35], physical co-sputtering[36], or the quenching of a liquid or gas elemental mixture prepared at a high temperature[22,37,38]. However, it is unclear whether these mixed nanostructures are thermodynamic alloys or kinetically-trapped structures. Besides, it remains difficult to synthesize ultrasmall nanoparticles at a thermodynamic state spanning a broad compositional range. To date, there is a lack of comprehensive experimental insights into how materials dimensions affect their thermodynamic phase-separation behavior and how this deviates from the bulk phase diagram. At the small length scales of nanomaterials and atomic clusters, the large proportion of surface atoms is a crucial factor in controlling material's thermodynamic state[37-41]. In particular, atoms on the terraces, edges, and corners possess fewer neighboring atoms than atoms in bulk, resulting in a decreased coordination number between immiscible elements and therefore a decreased enthalpy of mixing of the system. In addition, defects and structural relaxation in nanoparticles can relieve strain caused by the lattice and size mismatch of different elements[27,42,43], further influencing the thermodynamic state. In a previous experimental study, we have shown that the solubility between Au and Rh increases to ~10% in particles of size between 4-12 nm, as opposed to the < 1% solubility at the bulk scale[44]. Given the significant role of surface atoms in influencing the thermodynamic state of the materials[40,41], it is possible that by further decreasing

particle size, even immiscible elements may fully mix.

Here, to examine whether this immiscibility-to-miscibility transition occurs, we investigate the thermodynamic phase-separation behavior of two immiscible elements (Au and Rh) in a nanoparticle with compositions varying from 15% to 85% Au and of size between 4 and 1 nm. We show that unlike the bulk phase diagram, the phase-separation behavior of Au and Rh in a nanoparticle highly depends on the particle composition, size, and surface passivation. The miscibility gap between Au and Rh can be eliminated spanning the whole compositional range in the sub-2 nm size regime. First-principles calculations show that different surface adsorbates, present under synthesis conditions, can change the surface energies of Au and Rh sufficiently to cause a cross-over in thermodynamic phase stability.

Effect of particle size and composition on the phase-separation behavior

We chose Au and Rh as a model system because the two elements will segregate into two phases that are almost unary at temperature < 1000 °C (Fig. 1a)[11]. Both virtually pure phases adopt a face center cubic lattice structure (Fig. 1b), which simplifies the structural analysis of the binary system. The two elements are not air-sensitive, minimizing the influence of air-induced oxidation when characterizing the nanoparticles. In addition, Au and Rh have a large difference in atomic number, making them distinguishable by high-angle annular dark-field scanning transmission electron microscopy (HAADF-STEM) since HAADF-STEM image intensity is proportional to the atomic number ($I \propto Z^{1.7}$, Fig. 1c)[45]. To synthesize AuRh nanoparticles with desired size and composition, polymer micelles made of polystyrene-*b*-poly(2-vinylpyridine) with metal salt precursors coordinated to the pyridyl groups were used as nanoreactors to mediate the nanoparticle synthesis. The micelles were spin-coated on TEM grids with carbon support films. The grids were thermally annealed under flowing Ar/H_2 to decompose the polymer template, convert metal precursors into nanoparticles, and ensure that Au and Rh reach thermodynamic equilibrium (Supplementary Fig. 1).

The synthesized nanoparticles were characterized by aberration-corrected HAADF-STEM to assess the distribution of Au and Rh atoms and measured by energy dispersive X-ray spectroscopy (EDS) to determine the composition. Au and Rh phase separate into two domains in nanoparticles larger than 4 nm, as verified by the elemental mapping and the contrast of Au and Rh domains in the HAADF-STEM images (Fig. 1d, 1e, and Supplementary Fig. 2). To evaluate whether Au and Rh can be completely alloyed in a smaller-size particle, we first

explored $Au_{0.5}Rh_{0.5}$ with diameters specifically tailored between 4 and 1 nm (Fig. 1f). When the particle size is larger than 3 nm, the contrast between Au and Rh domains indicates that AuRh adopt a heterodimer structure. When the particle size is decreased into the range of 2.2-1.8 nm, the interface between Au and Rh domains become more diffusive. The interface eventually disappears in every particle of size less than 1.8 nm. We also performed simulation on the HAADF-STEM images of ~1.6 nm AuRh particles with dimeric or core-shell structures. These structural features can be clearly identified by HAADF-STEM (Supplementary Figs. 3-6), but has never been experimentally observed. As such, the HAADF-STEM characterization suggests that AuRh nanoparticles undergo a transition from phase-separation to alloy when the particles size is decreased from 4 to 1 nm, as schematically illustrated in Fig. 1g.

To further understand the size effect, we systematically synthesized and investigated AuRh nanoparticles with five different compositions in the size regime of 4-1 nm (Fig. 2). The average compositions of the five types of nanoparticles are $Au_{0.15}Rh_{0.85}$, $Au_{0.3}Rh_{0.7}$, $Au_{0.5}Rh_{0.5}$, $Au_{0.7}Rh_{0.3}$, and $Au_{0.85}Rh_{0.15}$, respectively (Fig. 2e and Supplementary Figs. 7-9). For this set of five samples, the mixing behavior of Au and Rh are highly dependent on both particle composition and size. When the particle composition is in the range of 30% to 70% Au (Fig. 2a, second to fourth column), the particles generally exhibit a transition from heterostructured, to intermediate, to alloyed when particle size changes from 4 to 1 nm. Specifically, nanoparticles of ~4 nm display a heterostructured state, where a sharp interface between Au and Rh can be clearly observed (Fig. 2a, highlighted by green squares). In contrast, nanoparticles of ~1.6 nm exhibit an alloyed structure, as evidenced by the disappearance of the interfaces and the even contrast in the STEM images (Fig. 2a, highlighted by blue squares). In the size regime between the heterostructured and alloyed states, the nanoparticles manifest an intermediate structure in which Au or Rh forms multiple domains in a single nanoparticle and the phase boundaries are less sharp (Fig. 2a, highlighted by red squares). Compared with these nanoparticles, no size-dependent transition is observed in nanoparticles composed of 15% or 85% Au. For these two specific compositions, Au and Rh can be alloyed in the entire 4-1 nm range (Fig. 2a, first and fifth column). Taken together, both particle composition and size affect the separation state between Au and Rh while a smaller particle size generally favors the mixing of them (Fig. 2a and Supplementary Fig. 10).

The three different mixing-states between Au and Rh (heterostructured, intermediate, and alloyed) are also confirmed by performing line-scan analyses on the atomic-resolution STEM

images. The line-scan profile across the interface of a heterostructured particle reveals the separation between bright atomic columns and dark atomic columns, which can be assigned to the single Au domain and Rh domain in the nanoparticle (Fig. 2b and Supplementary Fig. 11). A sharp interfacial region within about three atomic columns can be found in the nanoparticle. For an intermediate nanoparticle (Fig. 2c), the bright atomic columns indicative of Au-rich columns are randomly distributed in the line-scan profile, suggesting the formation of multiple Au or Rh domains in the particle due to the increased mixing level between Au and Rh. In the line-scan profile of an alloyed nanoparticle (Fig. 2d), the intensity of all atomic columns is relatively uniform, suggesting the well-mixed state between Au and Rh. In comparison with the three distinct states in AuRh nanoparticles, we also characterized pure Au and Rh nanoparticles in the size range of 4-1 nm (Supplementary Fig. 12). Their HAADF-STEM images exhibit homogenous contrast, confirming that the observation of phase separation-to-alloy transition is not an artifact caused by HAADF-STEM characterization.

Quantitative evaluation of the phase separation-to-alloy transition

To further understand the transition, we quantitatively assessed the mixing state between Au and Rh by analyzing the number and cross-sectional area of the minor element's domains in a nanoparticle, *i.e.*, the Au domains in a Rh-rich nanoparticle and the Rh domains in a Au-rich nanoparticle (Fig. 3 and Supplementary Figs. 13-21). An algorithm based on a random walk model was developed to detect the bright Au domains in the STEM images (Supplementary Fig. 13). The information of Rh domains can be extracted by subtracting the Au domains from the nanoparticle (Supplementary Fig. 14). Notably, for alloyed $Au_{0.15}Rh_{0.85}$ and $Au_{0.85}Rh_{0.15}$ (Fig. 3 and Supplementary Fig. 15d and 15e), the cross-sectional area of the minor element's domains is between 0.05-0.20 nm^2, suggesting that their cross-sectional area is about 1-4 atoms in an alloyed nanoparticle. In this work, we use 0.2 nm^2 as the critical cross-sectional area of domains to differentiate the alloyed and separated states of AuRh. For nanoparticles within the compositional range of 30% to 70% Au (Supplementary Fig. 15a-15c), a transition region can be identified for each different composition. In these regions, the nanoparticles start to adopt an intermediate structure that is neither heterostructured nor alloyed. Taking $Au_{0.5}Rh_{0.5}$ as an example (Fig. 3a and 3b), the number of Au domains in a nanoparticle persists at one and the Au domain area gradually decreases when the particle size is decreased from 4 to 2.2 nm, because $Au_{0.5}Rh_{0.5}$ has a heterodimer structure in this region. When the particle size falls in the range of

2.2-1.8 nm, the transition region for $Au_{0.5}Rh_{0.5}$, Au splits into several domains in a nanoparticle due to the enhanced Au-Rh mixing. Consequently, the number of Au domains increases from 1 to ~5 until a plateau is reached, and the cross-sectional area of Au domains decreases from 0.9 to ~0.2 nm^2, approaching the borderline of AuRh alloy. The Au domain area remains < 0.2 nm^2 in sub-1.8 nm $Au_{0.5}Rh_{0.5}$ nanoparticles due to the alloying of Au and Rh. The quantitative analysis corroborates that $Au_{0.5}Rh_{0.5}$ experiences a phase separation-to-alloy transition when particle size decreases, with the intermediate state occurring between 2.2-1.8 nm. For $Au_{0.3}Rh_{0.7}$ and $Au_{0.7}Rh_{0.3}$ nanoparticles (Supplementary Fig. 15a and 15c), a similar trend can be observed. The transition regions for $Au_{0.3}Rh_{0.7}$ and $Au_{0.7}Rh_{0.3}$ are 3.2-2.0 nm and 3.7-2.2 nm, respectively. The inverse miscibility relationship of Au-Rh in the $Au_{0.3}Rh_{0.7}$, $Au_{0.5}Rh_{0.5}$, and $Au_{0.7}Rh_{0.3}$ nanoparticles supports the conclusion that small material size can flip over the thermodynamic phase-separation behavior of immiscible elements.

The phase separation-to-alloy transition is also impacted by particle composition. In general, AuRh is more resistant to this transition when the particle contains a closer content of Au and Rh (Fig. 3c-3e and Supplementary Fig. 16). Fig. 3c shows the parallel comparison between the five compositions at a fixed particle size of ~3 nm. $Au_{0.5}Rh_{0.5}$ exhibits a heterodimer structure because of the highest repulsion energy between Au-Rh in this composition (Supplementary Fig. 22), that can overcome the size-induced mixing effect and lead to the phase-separated structure (Fig. 3c, third column). The mixing enthalpy of $Au_{0.3}Rh_{0.7}$ and $Au_{0.7}Rh_{0.3}$ are reduced by 16% over that of $Au_{0.5}Rh_{0.5}$ (Supplementary Fig. 22a). For these two compositions, both the interaction between Au and Rh and the surface effect are at work to dictate the phase-separation state. The nano-size effect increases the mixing capability between Au and Rh, while the moderate repulsion energy between them prevents their full alloying. Consequently, Au and Rh split into several domains (>0.2 nm^2) in $Au_{0.3}Rh_{0.7}$ and $Au_{0.7}Rh_{0.3}$ nanoparticles, respectively (Fig. 3c, second and fourth columns). For $Au_{0.15}Rh_{0.85}$ and $Au_{0.85}Rh_{0.15}$, the repulsion energy is reduced by 49% over that of $Au_{0.5}Rh_{0.5}$ (Supplementary Fig. 22a), resulting in a smaller obstacle for Au and Rh to mix. Quantitative analysis confirms that these two compositions prefer an alloyed structure, where Au or Rh form domains smaller than 0.2 nm^2 in the nanoparticles (Fig. 3c, first and fifth columns).

To combine all of our quantitative analysis, we plotted a size-dependent phase diagram of Au-Rh (Fig. 4). The experimental data points of heterostructured, intermediate, and alloyed particles are denoted by green △, red □, and blue ○, respectively. Compared with the large

miscibility gap in the Au-Rh bulk phase diagram, the gap is diminished in sub-4 nm AuRh particles and can be closed across the entire compositional range in the sub-2 nm size regime. With the decrease of particle size, AuRh nanoparticles exhibit a transition from heterostructured, to intermediate, to alloyed while the actual transition occurs in a different size region for different compositions. The closer the Au/Rh ratio is to an equimolar value, the smaller the particle size is needed to initiate this transition. The major factor that causes the thermodynamic behavior change can be attributed to the increased surface effect. When one considers nanoparticles in the sub-4 nm size regime, the fraction of surface atoms is exponentially increased to a considerable level (Supplementary Fig. 23), making them non-negligible from the thermodynamic perspective.

Theoretical analysis of the nanoscale phase-separation behavior

Semi-empirical models have been widely used to explain the nano-size effect on the mixing pattern of immiscible elements[39-41]. For nanoparticles, the undercoordinated atoms on the surface are considered to diminish the interaction between incompatible atoms like Au and Rh, which facilitates the alloying of elements. In comparison, computational simulations based on density functional theory (DFT) or molecular dynamics have predicted core-shell Au-Rh nanoparticles as the stable structure[21,46,47]. Notably, these models neglect surface passivation effects such as adsorption of environmental species, which are likely to react with the nanoparticle surface area during synthesis.

Given the different structures reported in literature, we developed models that treat different types of AuRh structures (heterodimer, alloy, and core-shell) to interpret how particle size, composition, and available adsorbates affect miscibility (Supplementary Fig. 24). DFT was used to calculate the surface energy of Au and Rh, the interfacial energy between Au and Rh, the interaction parameter of Au-Rh at different compositions (Supplementary Fig. 25), and the surface adsorption energy of various species such as CH_3 (Supplementary Table 1). The models were parameterized with the DFT calculations to calculate the total energy of AuRh nanoparticles and assess the thermodynamically stable configurations (see discussion following Supplementary Fig. 24 for details). The result confirms the size-dependent stability of each configuration in the Au-Rh nanoparticle system in agreement with the particles synthesized herein (Fig. 5). A smaller particle size leads to an enhanced surface effect that suppress the mixing enthalpy toward a more negative value and promotes alloying, while an equimolar

elemental ratio results in a maximized repulsion energy between Au-Rh and facilitates phase-separation. The alloying is also promoted by configurational entropy. However, the entropy change from separated to alloyed states is relatively small compared with the variation of enthalpy from bulk AuRh to ultrasmall particles (Supplementary Fig. 22), rendering entropy a minor factor in determining the mixing state. Notably, while the model confirms previous computational studies of Au-Rh nanoparticles in vacuum, which identify the core-shell configuration as the most stable structure[21,46,47], we also find that core-shell nanoparticles are not expected to be stable when surface passivation from environmental species are considered (Fig. 5 and Supplementary Figs. 22 and 24-28).

In a vacuum environment, the surface energy difference for Au and Rh is calculated to be -9.8 eV/nm^2. With this value, the model predicts that Au-Rh particles would strongly favor core-shell character with Au enriched on the surface (Fig. 5a). However, during synthesis, organic species may adsorb to the undercoordinated surface atoms, and are likely to remain although the nanoparticles are plasma-cleaned in O_2 and re-annealed in H_2. While the bare surface energy of Au is lower than that of Rh, adsorbates tend to bind more strongly to Rh than Au surfaces (Supplementary Table 1). Therefore, surface passivation has the effect of reducing the difference in surface energies of each element, thereby destabilizing the core-shell phase and inducing a phase transformation from the core-shell to heterodimer or alloy geometry (Fig. 5 and Supplementary Fig. 26 and 27). According to a screening of several possible adsorbates, there are several organic adsorbates that bind strongly enough to each surface to induce this transformation (Supplementary Table 1 and Fig. 27). The predicted equilibrium structure of passivated ultrasmall Au-Rh nanoparticles at 500°C is presented in Fig. 5b, which is in good agreement with the experimental findings. Taken together, our experimental study combined with the theoretical analysis show that the thermodynamic phase stability of immiscible elements can change due to the size-dependent, surface environment-induced effects.

Conclusions

We have systematically explored the phase-separation of Au and Rh in a nanoparticle. Despite the high incompatibility between Au and Rh in a bulk material, miniaturizing AuRh materials to the nano and cluster size regime can switch their miscibility relationship from immiscible to fully alloyable, as we have demonstrated for sub-2 nm AuRh alloy nanoparticles

across a broad compositional range. We have found that the change of mixing behavior is affected by particle size, composition, and surface passivation. Surface passivation reduces the relative energy of Rh with respect to Au, destabilizing core-shell geometries and instead favoring the heterodimer and alloy phases. In passivating environments, a thermodynamic model parametrized by DFT calculations validates that Au and Rh will alloy at ultrasmall sizes. Our work quantitatively prove that the bulk phase diagram does not necessarily apply to nanoscale materials. The experimental results call for the exploration of the phase-separation behavior of multielement nanosystems, before conclusively interpreting their thermodynamic structure. Understanding the thermodynamic behavior of multielement nanoparticles will open up the ability to engineer the structures and properties of multielement nanoparticles for real-life applications.

Acknowledgements

This work was supported by Director, Office of Science, Office of Basic Energy Sciences, Chemical Sciences, Geosciences, & Biosciences Division, of the US Department of Energy under Contract DE-AC02-05CH11231, FWP CH030201 (Catalysis Research Program). Work at the Molecular Foundry was supported by the Office of Science, Office of Basic Energy Sciences, of the U.S. Department of Energy under Contract No. DE-AC02-05CH11231. This work made use of TEM facilities at the Cornell Center for Materials Research (CCMR) which are supported through the National Science Foundation Materials Research Science and Engineering Center (NSF MRSEC) program (DMR-1719875). P.-C.C. acknowledges support from Kavli ENSI Heising-Simons Fellowship. J.J. acknowledges fellowship support from Suzhou Industrial Park. Y.Y acknowledges support from Miller Fellowship. C.A.M. acknowledges the National Defense Science and Engineering Graduate (NDSEG) fellowship and the Kavli ENSI Graduate Student Fellowship for financial support. This research used resources of the National Energy Research Scientific Computing Center, a DOE Office of Science User Facility supported by the Office of Science of the U.S. Department of Energy under Contract No. DE-AC02-05CH11231 using NERSC award BES-ERCAP0024004.

Author Contributions

P.-C.C. and P.Y. conceived the ideas and designed the experiments. P.-C.C. performed nanoparticle synthesis and conducted electron microscopy characterization. M.G. designed the quantitative analysis algorithm. P.-C.C. and M.G. analyzed electron microscopy characterization data and performed STEM image simulation. C.A.M. and K.A.P. performed the DFT calculations and theoretical analysis. C.S., J.J., Y.Y. and A.L.M. discussed the experimental results. P.-C.C., M.G., and P.Y. wrote the manuscript with editorial input from the other authors. P.Y. supervised the project.

Competing interests

The authors declare no competing interests.

References

1. Xie, C. L. *et al.* Tandem Catalysis for CO_2 Hydrogenation to C2-C4 Hydrocarbons. *Nano Lett.* **17**, 3798-3802 (2017).
2. Lewis, R. J. *et al.* Highly efficient catalytic production of oximes from ketones using in situ-generated H_2O_2. *Science* **376**, 615-620 (2022).
3. Yang, T. *et al.* Ultrahigh-strength and ductile superlattice alloys with nanoscale disordered interfaces. *Science* **369**, 427-432 (2020).
4. Shi, P. J. *et al.* Hierarchical crack buffering triples ductility in eutectic herringbone high-entropy alloys. *Science* **373**, 912-918 (2021).
5. He, Q. F. *et al.* A highly distorted ultraelastic chemically complex Elinvar alloy. *Nature* **602**, 251-257 (2022).
6. Oh, N. R. *et al.* Double-heterojunction nanorod light-responsive LEDs for display applications. *Science* **355**, 616-619 (2017).
7. Ibrar, M. & Skrabalak, S. E. Designer Plasmonic Nanostructures for Unclonable Anticounterfeit Tags. *Small Struct.* **2**, 2100043 (2021).
8. Jiang, B. B. *et al.* High-entropy-stabilized chalcogenides with high thermoelectric performance. *Science* **371**, 830-834 (2021).
9. Jiang, B. B. *et al.* High figure-of-merit and power generation in high-entropy GeTe-based thermoelectrics. *Science* **377**, 208-213 (2022).
10. Pendharkar, M. *et al.* Parity-preserving and magnetic field-resilient superconductivity in InSb nanowires with Sn shells. *Science* **372**, 508-511 (2021).
11. H. Okamoto, M. E. Schlesinger, E. M. Mueller, Eds, *Alloy Phase Diagrams*, ASM Handbook Vol.3. ASM International: Materials Park, OH, U.S.A., 2016.
12. Loffler, T. *et al.* Discovery of a Multinary Noble Metal-Free Oxygen Reduction Catalyst. *Adv. Energy Mater.* **8**, 1802269 (2018).
13. Kusada, K. *et al.* Nonequilibrium Flow-Synthesis of Solid-Solution Alloy Nanoparticles: From Immiscible Binary to High-Entropy Alloys. *J. Phys. Chem. C* **125**, 458-463 (2021).
14. Chen, Y. F. *et al.* Synthesis of monodisperse high entropy alloy nanocatalysts from core@shell nanoparticles. *Nanoscale Horiz.* **6**, 231-237 (2021).
15. Wang, C. Y. *et al.* Facet-Dependent Deposition of Highly Strained Alloyed Shells on Intermetallic Nanoparticles for Enhanced Electrocatalysis. *Nano Lett.* **17**, 5526-5532 (2017).
16. Chen, P. C. *et al.* Polyelemental nanoparticle libraries. *Science* **352**, 1565-1569 (2016).
17. Chen, P. C. *et al.* Interface and heterostructure design in polyelemental nanoparticles. *Science* **363**, 959-964 (2019).
18. Chen, P. C. *et al.* Chain-End Functionalized Polymers for the Controlled Synthesis of Sub-2 nm Particles. *J. Am. Chem. Soc.* **142**, 7350-7355 (2020).
19. Fenton, J. L., Steimle, B. C. & Schaak, R. E. Tunable intraparticle frameworks for creating complex heterostructured nanoparticle libraries. *Science* **360**, 513-517 (2018).
20. Steimle, B. C., Fenton, J. L. & Schaak, R. E. Rational construction of a scalable heterostructured nanorod megalibrary. *Science* **367**, 418-424 (2020).
21. Piccolo, L. *et al.* Understanding and controlling the structure and segregation behaviour of AuRh nanocatalysts. *Sci. Rep.* **6**, 35226 (2016).
22. Chen, P.-C. *et al.* Chemical and Structural Evolution of AgCu Catalysts in Electrochemical CO_2 Reduction. *J. Am. Chem. Soc.* **145**, 10116-10125, (2023).

23. Wang, B. *et al.* General synthesis of high-entropy alloy and ceramic nanoparticles in nanoseconds. *Nat. Synth.* **1**, 138-146 (2022).
24. Yang, C. L. *et al.* Sulfur-anchoring synthesis of platinum intermetallic nanoparticle catalysts for fuel cells. *Science* **374**, 459-464 (2021).\
25. Feng, G. *et al.* Sub-2 nm Ultrasmall High-Entropy Alloy Nanoparticles for Extremely Superior Electrocatalytic Hydrogen Evolution. *J. Am. Chem. Soc.* **143**, 17117-17127 (2021).
26. Buendia, F., Vargas, J. A., Johnston, R. L. & Beltran, M. R. Study of the stability of small AuRh clusters found by a Genetic Algorithm methodology. *Comput. Theor. Chem.* **1119**, 51-58 (2017).
27. Rahm, J. M. & Erhart, P. Understanding Chemical Ordering in Bimetallic Nanoparticles from Atomic-Scale Simulations: The Competition between Bulk, Surface, and Strain. *J. Phys. Chem. C* **122**, 28439-28445 (2018).
28. Christensen, A., Stoltze, P. & Norskov, J. K. Size Dependence of Phase-Separation in Small Bimetallic Clusters. *J. Phys. Condens. Matter* **7**, 1047-1057 (1995).
29. Fevre, M., Le Bouar, Y. & Finel, A. Thermodynamics of phase-separating nanoalloys: Single particles and particle assemblies. *Phys. Rev. B* **97**, 195404 (2018).
30. Srivastava, C., Chithra, S., Malviya, K. D., Sinha, S. K. & Chattopadhyay, K. Size dependent microstructure for Ag-Ni nanoparticles. *Acta Mater.* **59**, 6501-6509 (2011).
31. Kusada, K., Yamauchi, M., Kobayashi, H., Kitagawa, H. & Kubota, Y. Hydrogen-Storage Properties of Solid-Solution Alloys of Immiscible Neighboring Elements with Pd. *J. Am. Chem. Soc.* **132**, 15896-15898 (2010).
32. Zhang, Q. *et al.* Selective control of fcc and hcp crystal structures in Au-Ru solid-solution alloy nanoparticles. *Nat. Commun.* **9**, 510 (2018).
33. Zhang, H., Wang, L., Lu, L. & Toshima, N. Preparation and Catalytic Activity for Aerobic Glucose Oxidation of Crown Jewel Structured Pt/Au Bimetallic Nanoclusters. *Sci. Rep.* **6**, 30752 (2016).
34. Toshima, N. & Hirakawa, K. Polymer-Protected Bimetallic Nanocluster Catalysts Having Core/Shell Structure for Accelerated Electron Transfer in Visible-Light-Induced Hydrogen Generation. *Polym. J.* **31**, 1127-1132 (1999).
35. Toshima, N. & Yonezawa, T. Bimetallic nanoparticles-novel materials for chemical and physical applications. *New J. Chem.* **22**, 1179-1201 (1998).
36. Meischein, M. *et al.* Elemental (im-)miscibility determines phase formation of multinary nanoparticles co-sputtered in ionic liquids. *Nanoscale Adv.* **4**, 3855-3869 (2022).
37. Rajeeva, B. B. *et al.* Accumulation-Driven Unified Spatiotemporal Synthesis and Structuring of Immiscible Metallic Nanoalloys. *Matter* **1**, 1606-1617 (2019).
38. Feng, J. C. *et al.* Unconventional Alloys Confined in Nanoparticles: Building Blocks for New Matter. *Matter* **3**, 1646-1663 (2020).
39. Qi, W. H. & Wang, M. P. Size effect on the cohesive energy of nanoparticle. *J. Mater. Sci. Lett.* **21**, 1743-1745 (2002).
40. Xiong, S. Y., Qi, W. H., Huang, B. Y. & Wang, M. P. Size-, Shape- and Composition-Dependent Alloying Ability of Bimetallic Nanoparticles. *ChemPhysChem* **12**, 1317-1324 (2011).
41. Qi, W. H., Huang, B. Y. & Wang, M. P. Size and shape-dependent formation enthalpy of binary alloy nanoparticles. *Physica B* **404**, 1761-1765 (2009).
42. Sneed, B. T., Young, A. P. & Tsung, C. K. Building up strain in colloidal metal nanoparticle

catalysts. *Nanoscale* **7**, 12248-12265 (2015).
43. R. Ferrando, *Structure and Properties of Nanoalloys*. Elsevier: Amsterdam, Netherlands, 2016.
44. Chen, P. C. *et al.* Revealing the Phase Separation Behavior of Thermodynamically Immiscible Elements in a Nanoparticle. *Nano Lett.* **21**, 6684-6689 (2021).
45. Sohlberg, K., Pennycook, T. J., Zhou, W. & Pennycook, S. J. Insights into the physical chemistry of materials from advances in HAADF-STEM. *Phys. Chem. Chem. Phys.* **17**, 3982-4006 (2015).
46. Vanzan, M., Jones, R. M., Corni, S., D'Agosta, R. & Baletto, F. Exploring AuRh Nanoalloys: A Computational Perspective on the Formation and Physical Properties. *ChemPhysChem* **23**, e202200035 (2022).
47. Valizadeh, Z. & Abbaspour, M. Surface energy, relative stability, and structural properties of Au-Pt, Au-Rh, Au-Cu, and Au-Pd nanoclusters created in inert-gas condensation process using MD simulation. *J. Phys. Chem. Solids* **144**, 109480 (2020).

Methods

Materials

Gold(III) chloride and rhodium(III) nitrate hydrate were purchased from Sigma-Aldrich, Inc. and used without further purification. Polystyrene-*b*-poly(2-vinylpyridine) (PS-*b*-P2VP, Mn = 34-*b*-18 kg/mol, dispersity = 1.11) was purchased from Polymer Source, Inc and used as received. Anhydrous toluene and methanol were purchased from Sigma-Aldrich, Inc. and used as received. Nickel and gold TEM grids with a 3-nm ultrathin carbon film coated on a lacey carbon support were purchased from Ted Pella, Inc.

Synthesis of AuRh nanoparticles in micelle reactors

Polymer micelles were prepared by dissolving 5 mg of PS-*b*-P2VP in 1 mL of toluene. $AuCl_3$ was first dissolved in 10 μL of methanol and then added to the micelle solution. The mixture solution was sonicated using a tip sonicator (SONICS VCX 500, 2 mm tip) at a 20% amplitude for 60 s and at a 40% amplitude for 60 s, successively, to facilitate the dispersion of $AuCl_3$ in the micelles. After that, the micelle solution was stirred at room temperature for 6 h. $Rh(NO_3)_3$ was dissolved in 10 μL of methanol and added to the micelle solution to get a desired molar ratio between $AuCl_3$ and $Rh(NO_3)_3$. The resulting mixture solution was further stirred at room temperature for 12 h prior to use. For the synthesis of $Au_{0.15}Rh_{0.85}$, $Au_{0.3}Rh_{0.7}$, $Au_{0.5}Rh_{0.5}$, $Au_{0.7}Rh_{0.3}$, and $Au_{0.85}Rh_{0.15}$ nanoparticles, the molar ratios between Au and Rh salts were set to 1:1, 2:1, 3:1, 5:1, and 8:1, respectively. The molar ratio between pyridyl groups and total metal precursors was controlled between 32:1 to 128:1 in order to obtain nanoparticles of size from 4-1 nm. To convert micelles to nanoparticles, the solution of precursor-loaded micelles was first spin-coated on a TEM grid at a spin rate of 4000 rpm. The TEM grid was treated with O_2 plasma (Harrick Plasma Cleaner, PDC-32G) for 7 min, followed by thermal annealing under flowing Ar/H_2 (90/10, v/v) in a tube furnace. The annealing conditions were designed as follows: ramp to 150 °C in 1 h, hold at 150 °C for 4 h, ramp to 250 °C in 1 h, hold at 250 °C for 4 h, ramp to 400 °C in 1 h, hold at 400 °C for 1 h, ramp to 500 °C in 1 h, hold the grids at 500 °C for 12 h, and finally cool down to room temperature in 5 h. The stepwise annealing between 150-400 °C can facilitate the nucleation, growth, and coarsening of the metal species in each micelle reactor to form a single nanoparticle. The last annealing step at 500°C decomposes the micelles and ensures that AuRh reaches a thermodynamic equilibrium. Plasma cleaning (Fischione plasma cleaner, Model 1020) under Ar/O_2 (75/25, v/v) was applied on the TEM grids for 10s to remove the carbon residues formed on the synthesized nanoparticles. The TEM grids were then annealed at 500 °C under flowing Ar/H_2 (90/10, v/v) for another 12 h and cooled down to room temperature in 12 h before characterization.

Characterization

A Hitachi 7650 transmission electron microscope (TEM) operated at 100 kV was used to record low-resolution TEM images of the polymer micelles and nanoparticles. Energy-dispersive X-ray spectroscopy (EDS) and scanning transmission electron microscopy (STEM) characterizations of the nanoparticles were performed on a Thermo Fisher Scientific Titan 60-300 transmission electron microscope at an acceleration voltage of 300 kV. The electron microscope is equipped with four silicon drift EDS detectors with a total solid angle of 0.7 steradians. The Lα peaks of Au and Rh in the EDS spectra were used for elemental mapping and composition quantification of the nanoparticles. The atomic compositions were calculated using the standardless Cliff-Lorimer correction method. Each EDS map was built based on accumulation of 150 frames with

pixel dwell-time of 8 μs. Bruker Esprit software was used for background subtraction in the EDS maps. Electron energy loss spectroscopy (EELS) maps of the nanoparticles were acquired on a fifth-order aberration-corrected STEM (Cornell Nion UltraSTEM) operated at 100 keV with a beam convergence semi-angle of 30 mrad. EELS spectral images were acquired with a 0.25 eV/channel energy dispersion (energy resolution, 1.0 eV) in a Gatan spectrometer with a size of 100×100 pixels and an acquisition time of 10 ms/pixel. The Rh and Au elemental maps were extracted using their $M_{5,4}$ edges from the EELS spectrum images and processed using principal component analysis (PCA, 3 components) and the linear combination of power law (LCPL) in ImageJ software to subtract the background. Atomic-resolution HAADF-STEM characterization of the nanoparticles were conducted on TEAM0.5, an aberration-corrected Thermo Fisher Scientific Titan 80-300 TEM, at an acceleration voltage of 200 kV. Typical aberration coefficients used for imaging are C1=-2.15 nm, A1=1.68 nm, A2=14.5 nm, B2=14.9 nm, C3=-228 nm, A3=120 nm, S3=199 nm, A4=4.19 μm, D4=3.03 μm, B4=4.28 μm, C5=-90.58 μm, A5=118 μm. The HAADF-STEM images were acquired using a high-angle annular dark-field detector with collection semi-angles from 58 to 265 mrad and a probe convergence semi-angle of 30 mrad. The probe size is ~0.5 Å. The beam current was set to 70 pA for the imaging of 2-4 nm nanoparticles and was set to ~6 pA for the imaging of 1-2 nm nanoparticles. All HAADF-STEM images were recorded in a 1024×1024 pixels format at a pixel dwell-time of 3 μs. The electron dose rate was about 780 $e^-/Å^2s$. Short-pass filter was applied in the Fourier space for the images of sub-2nm AuRh particles to improve image quality. A typical filter threshold is 1/1.5 or 1 $Å^{-1}$, corresponding to 1.5 or 1 Å. STEM image simulation of the single Au and Rh atoms was performed using the QSTEM software[48]. The experimental microscope parameters described above were used as parameters for the image simulation.

Quantitative analysis of HAADF-STEM images

An algorithm based on a random walk model was developed to detect the bright Au domains in STEM images. The algorithm first automatically detects a nanoparticle from the full frame of a STEM image and crops the nanoparticle out for analysis. A threshold value that is the average intensity of the bright and dark domains in STEM images is selected to distinguish Au-rich and Rh-rich domains. A brush size which is approximately equals to the size of atom and a step size which is equal to the size of the brush are selected. The following random walk model is then used to identify all the bright domains that correspond to Au. (1) In a typical round of random walk analysis, the algorithm first identifies the brightest pixel in the image and use it as a probing pixel. (2) Around the probing pixel, it calculates the pixel intensities of eight patches (of the size of the brush) with a step-size away from the probing pixel. If any patch has an intensity above the threshold value, it identifies that patch to be a propagation candidate, which will be selected as the new probing pixel in the next propagation step. (3) After each step, a group of propagation candidates will be used as the new probing pixels to start the next propagation step. (4) We set the number of patches around every probing pixel in each propagation step to be eight, which proves to be sufficient to cover a continuous domain. (5) The propagation of probing pixels is ended when the algorithm cannot find any connected patch with intensity above the threshold value. Then the enclosed map of the propagation trajectory is recognized as a domain. (6) After one round of random walk analysis, the recognized bright domains will be excluded from the image, so that those pixels will not be recognized as a propagation candidate in the future analysis. (7) The next round of random walk analysis then starts to look for another brightest

pixel that is outside of the domain identified before, and this pixel will be the starting pixel for a new domain. (8) We repeat the domain search for 50 times. In principle, all bright domains within a nanoparticle can be recognized. After all the random walk analyses, any pixel within a particle identified as a part of a domain will be marked by intensity 1 and the other pixels will be given an intensity of 0. We binarize the image and the number of domains is analyzed by the function in MATLAB Image Processing Toolbox, *i.e.*, bwconncomp(), which finds and counts the connected components in the binary image. The size and amount of Au domains in a nanoparticle image can then be calculated (Supplementary Fig. 13). The information of Rh domains can also be extracted by subtracting the Au domains from the entire nanoparticle (Supplementary Fig. 14).

DFT calculations and theoretical analysis

All DFT calculations were performed with the VASP 6 package[49], with the generalized gradient approximation (GGA) and the Perdew-Burke-Ernzerhof (PBE) exchange-correlation functional, the projected augmented wave (PAW) method[50,51], and spin polarization. All calculations of bulk phases were performed with a Brillouin zone sampling of 10x10x10. Slab and interface calculations were performed with a Brillouin zone sampling of 4x4x1 with the longest cell dimension having a sampling of 1. To avoid spurious interactions in the periodic boundary conditions, all distances between non-interacting surfaces were set to be greater than 10Å with vacuum separation. DFT calculated values of the AuRh system, including surface energy, interfacial energy, and interaction parameters, were used to evaluate the total energy of nanoparticles of different size, composition, and configurations.

Data Availability

The data supporting the findings of this study are available within the article and its Supplementary Information, and are available from the corresponding author on reasonable request.

Code Availability

The source codes of the algorithm for HAADF-STEM image analysis are available on the Zenodo website (DOI: 10.5281/zenodo.10510952).

Methods-only references

48. Koch, C. T. Determination of core structure periodicity and point defect density along dislocations. Ph.D. Thesis, Arizona State University, Tempe, AZ, U.S.A., 2002.
49. Kresse, G. & Furthmuller, J. Efficient iterative schemes for ab initio total-energy calculations using a plane-wave basis set. *Phys. Rev. B* **54**, 11169-11186 (1996).
50. Kresse, G. & Joubert, D. From ultrasoft pseudopotentials to the projector augmented-wave method. *Phys. Rev. B* **59**, 1758-1775 (1999).
51. Perdew, J. P., Burke, K. & Ernzerhof, M. Generalized Gradient Approximation Made Simple. *Phys. Rev. Lett.* **77**, 3865-3868 (1996).

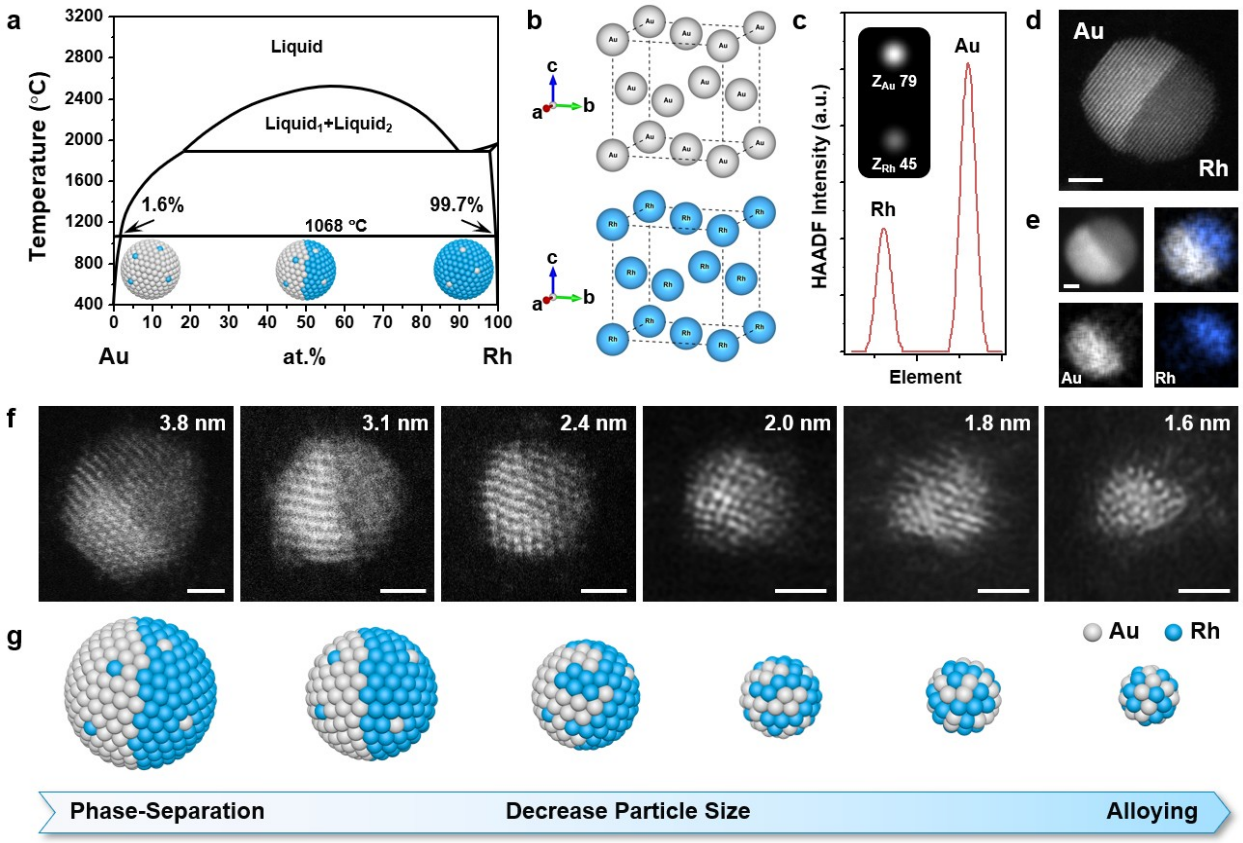

Fig. 1. Overview of the size-dependent miscibility relationship between Au and Rh. (**a**) Bulk phase diagram of Au-Rh binary system (*11*). (**b**) Crystal structure of Au metal and Rh metal. The grey and blue atoms represent Au and Rh, respectively. (**c**) Simulated HAADF-STEM intensity profile of single Au and Rh atoms. Inset is the simulated HAADF-STEM image of single Au and Rh atoms. (**d,e**) HAADF-STEM images and EDS elemental mapping of AuRh nanoparticles with size larger than 4 nm. Scale bars, 2 nm. (**f**) HAADF-STEM images of AuRh nanoparticles of size decreased from 4 to 1 nm. (**g**) Schematic illustration of the transition from phase-separation to alloying in 4-1 nm AuRh nanoparticles.

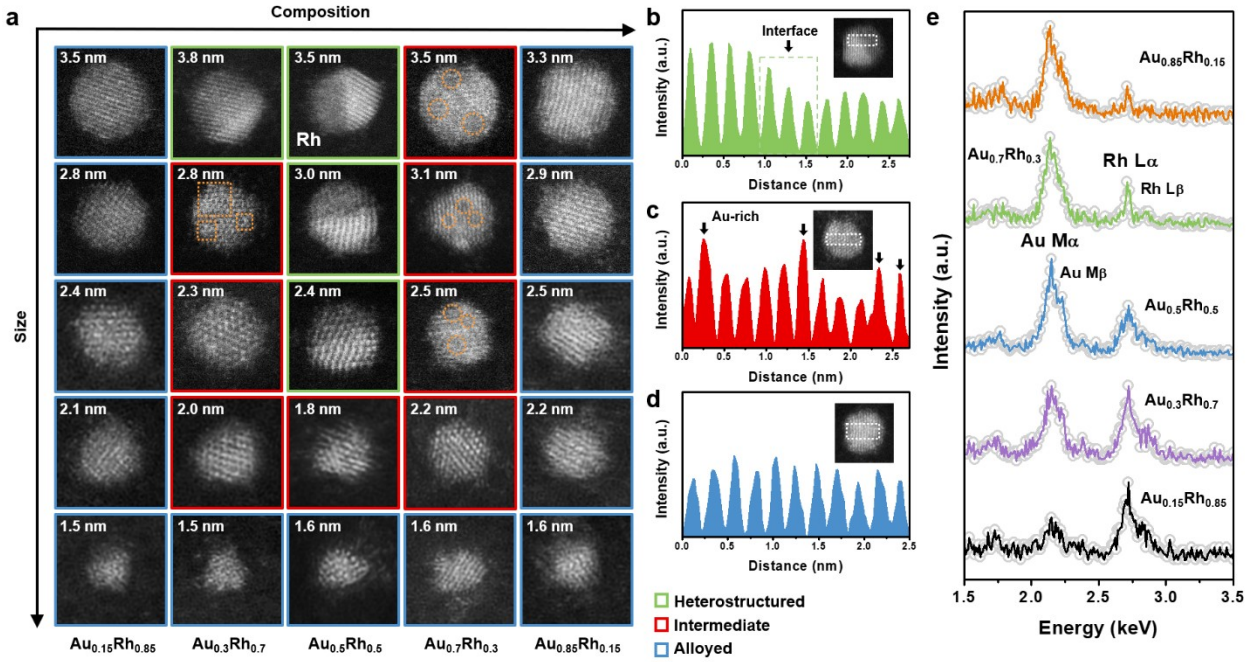

Fig. 2. Close of the miscibility gap between Au and Rh at the nano- and cluster length scales. (**a**) HAADF-STEM images of AuRh nanoparticles with composition changing from 15% Au to 85% Au (atomic ratio) and of size between 4 and 1 nm. Orange squares highlight the Au domains split in the nanoparticles. Orange circles highlight the Rh domains split in the nanoparticles. (**b-d**) Line-scan profiles extracted from the HAADF-STEM images of AuRh nanoparticles possessing different Au-Rh mixing states, *i.e.*, heterostructured (b), intermediate (c), and alloyed (d). Insets are the HAADF-STEM images of the nanoparticles. The line-scan curves are plotted based on the region highlighted by the white rectangular lines (see Fig. S11 for details). (**e**) EDS spectra of the five types of AuRh nanoparticles with different compositions.

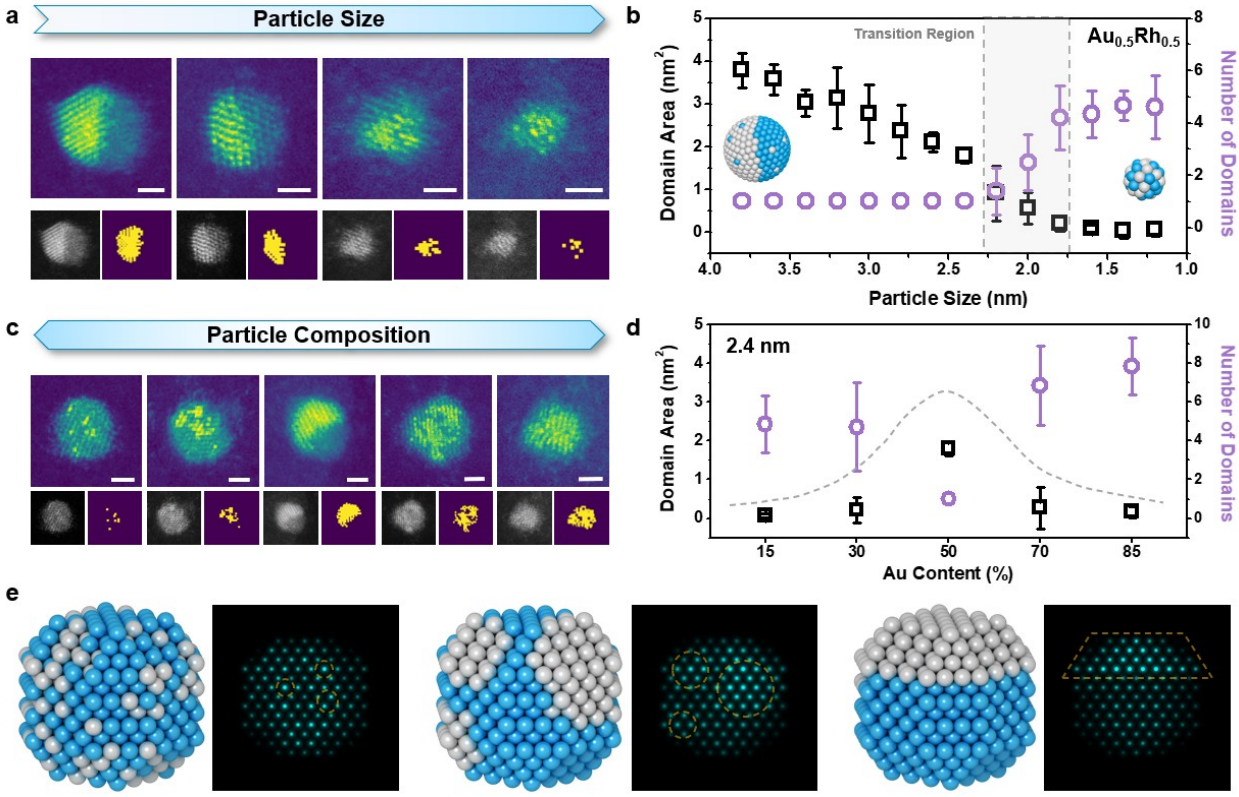

Fig. 3. Effect of particle size and composition on the phase-separation behavior between Au and Rh. (**a**) Size-dependent phase-separation in $Au_{0.5}Rh_{0.5}$ nanoparticles of size from 4 to 1 nm. Scale bars, 1 nm. Bottom row: HAADF-STEM images of the nanoparticles and corresponding image analysis showing the Au domains in the particles. Top row: HAADF-STEM images with the Au domains highlighted. (**b**) Dependence of the number and cross-sectional area of Au domains in $Au_{0.5}Rh_{0.5}$ nanoparticles on the nanoparticle size. The shaded grey region outlines the transition region. For each data point, the sample size is 20 particles. (**c**) Composition-dependent phase-separation of Au and Rh in nanoparticles of size about 3 nm. Scale bars, 1 nm. From the left to the right, the particle compositions are $Au_{0.15}Rh_{0.85}$, $Au_{0.3}Rh_{0.7}$, $Au_{0.5}Rh_{0.5}$, $Au_{0.7}Rh_{0.3}$, and $Au_{0.85}Rh_{0.15}$, respectively. (**d**) Dependence of the number and cross-sectional area of minor element's domains on the particle composition at a fixed particle size. Dashed lines depict the change of the domain area as guides for the eye. For each data point, the sample size is 20 particles. (**e**) Simulated HAADF-STEM images and corresponding models of $Au_{0.3}Rh_{0.7}$ particles with an alloyed, intermediate, or heterostructured state. Grey: Au atoms. Blue: Rh atoms. Orange circles and trapezoid highlight the distribution of Au atoms in the nanoparticles.

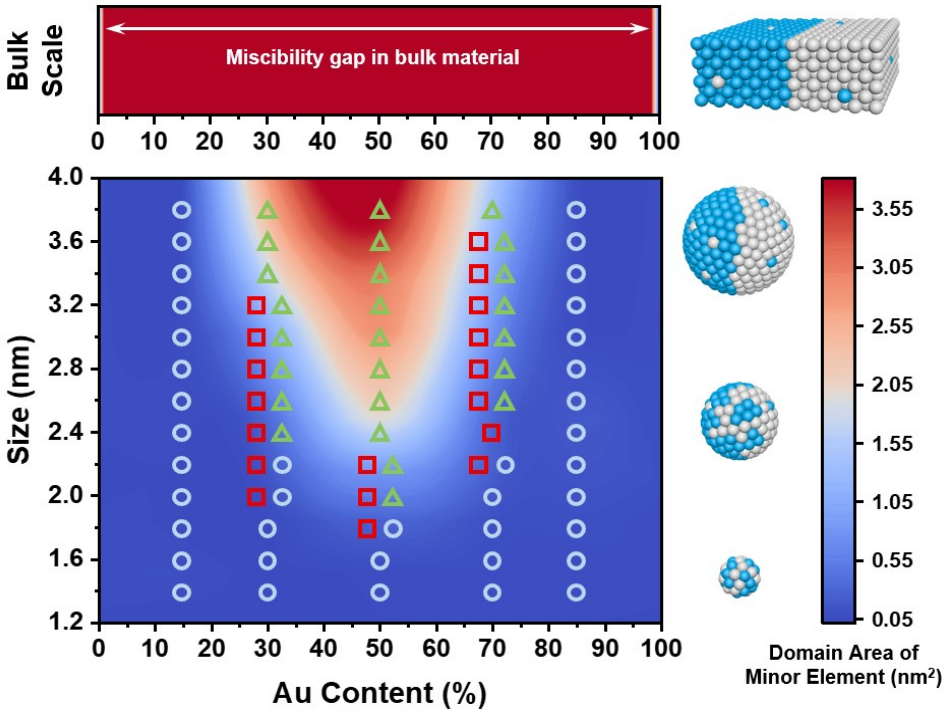

Fig. 4. Experimental Au-Rh phase diagram at the nano- and cluster length scales and its comparison with the bulk miscibility gap between Au-Rh. The phase map is projected based on the quantitative analysis of the cross-section area of the minor element domains, *i.e.*, Au domains in Rh-rich nanoparticles ($Au_{0.15}Rh_{0.85}$, $Au_{0.3}Rh_{0.7}$, and $Au_{0.5}Rh_{0.5}$), and Rh domains in Au-rich nanoparticles ($Au_{0.7}Rh_{0.3}$ and $Au_{0.85}Rh_{0.15}$). The experimentally observed data points of alloyed (○, light blue), intermediate (□, red), and heterostructured (△, green) nanoparticles are shown on the map. The schematic illustration depicts the transition from phase-separation to alloying in AuRh nanoparticles.

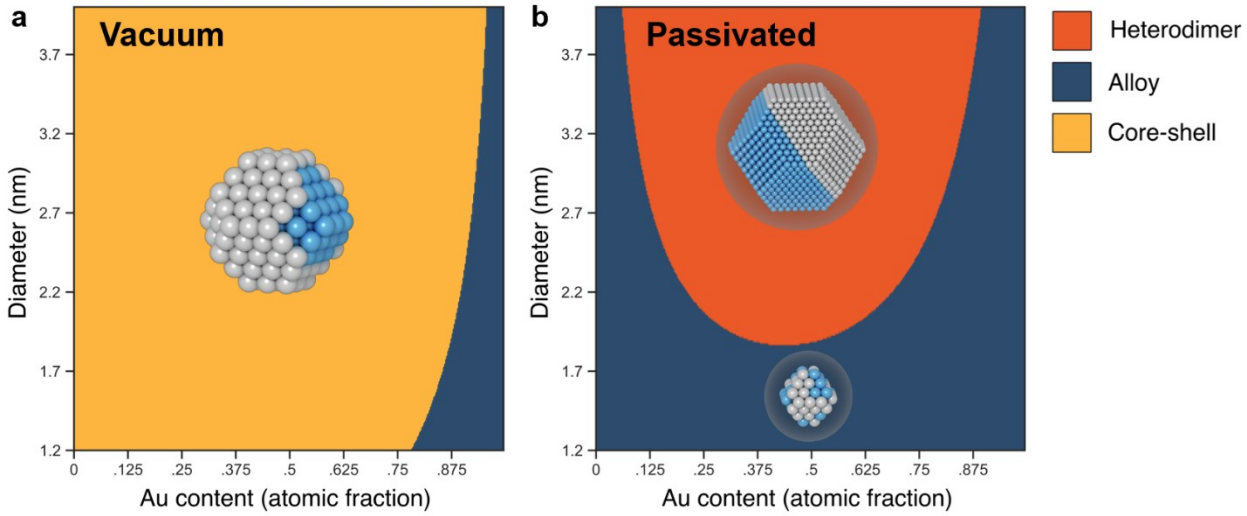

Fig. 5. Theoretical phase diagrams of the thermodynamic configurations of AuRh nanoparticles. (**a**) Size-dependent phase diagram expected for AuRh particles in ultra-high vacuum environments. Yellow phase: core-shell; Dark blue phase: alloy. (**b**) Size-dependent phase diagram expected with passivated surfaces of AuRh. Red phase: heterostructure; Dark blue phase: alloy. Each diagram is for the particles at 500˚C. Phase diagrams for the system with different passivation strengths and at variable temperatures are included in Fig. S27 and S28. In the inset models of core-shell, heterodimer, and alloy configurations, the grey atoms are Au and the blue atoms are Rh. The theoretical phase diagram with passivated surfaces matches well with the observed phases in Fig. 4.